

A chiral spin-photon interface for scalable on-chip quantum-information processing

Immo Söllner,^{*} Sahand Mahmoodian,^{*} Alisa Javadi, and Peter Lodahl[†]
Niels Bohr Institute, University of Copenhagen, Blegdamsvej 17, DK-2100 Copenhagen, Denmark
(Dated: January 5, 2023)

Single electron spins confined in semiconductor quantum dots are excellent candidates for stationary qubits enabling fast initialization, optical manipulation, and read out [1–5]. Quantum dots can be efficiently interfaced with photonic nanostructures to achieve light-matter entanglement [6] or deterministic photon-emitter coupling [7], which are main requirements for photonic quantum-information processing [8]. Furthermore, an efficient interface of long-lived spins and photons [9, 10] would be required for scalable quantum architectures. Here we propose a photonic-crystal waveguide that allows the deterministic interfacing of quantum-dot spins with nanophotonic waveguides through a chiral interaction. This chiral spin-photon interface features highly-directional photon emission for spin read-out and spin-path entanglement. Based on spin dependent directional scattering, we propose an all-solid-state and scalable controlled NOT gate implemented on a photonic chip. The protocol can be implemented with current technology thereby potentially leading to new realms for scalable photonic quantum-information processing based on integrated photonic circuits.

An efficient interface between quantum dot (QD) spins and photons is highly requested for quantum-information processing since it enables combining the favorable properties of spins (long-lived coherence) and photons (robust and easy manipulation). Achieving this with photonic nanostructures requires that the local mode profile is circularly polarized in order to couple to charged QD transitions. We propose a new photonic-crystal waveguide (PCW) design whose modes have a broadband in-plane circular polarization that efficiently couples orthogonal circularly polarized transitions of a QD to counter-propagating modes. This constitutes a *chiral spin-photon interface* in a waveguide. We show that narrow-band single photons acquire a π -phase shift in transmission when scattering off a QD transition in this waveguide. By combining the π -phase shift of the scattering process with coherent control of the spin ground state of a charged exciton, the chiral interface may be a central building block for scalable quantum-information processing integrated on a photonic chip. In particular, we demonstrate the potential for single-shot spin read-out of a charged QD and a single photon quantum non-demolition detector. Combining these two processes, a controlled NOT gate for photonic qubits can be realized, which is the

basis for a scalable quantum network.

We first discuss the coupling of the QD to a waveguide with in-plane circularly polarized modes. To quantify the degree of coupling to circular dipoles we project the field on right and left circular polarization basis vectors and use this to calculate decay rates for coupling to right and left propagating waveguide modes, Γ_R and Γ_L , respectively. Due to time reversal symmetry, the electric fields of the forward propagating mode in the waveguide with wavevector $k\hat{x}$ and the backward propagating mode with wavevector $-k\hat{x}$ obey $\mathbf{E}_{-k}(\mathbf{r}) = \mathbf{E}_k^*(\mathbf{r})$, where x is the direction along the waveguide. A circularly polarized dipole at a position of pure circular in-plane polarization thus only couples to a mode propagating in a single direction, while the orthogonal dipole emits into the counter-propagating mode. The combined QD-waveguide system can thus exhibit chiral behaviour even though the waveguide itself is not chiral.

The figures of merit for such a structure are the directionality factor F_{dir} and the directional β -factor

$$\beta_{\text{dir}} = \frac{\max[\Gamma_R, \Gamma_L]}{\Gamma_{\text{wg}} + \gamma_{\text{rad}}}. \quad (1)$$

Here, $\Gamma_{\text{wg}} = \Gamma_L + \Gamma_R$ and γ_{rad} is the coupling to non-guided radiation modes. Therefore β_{dir} quantifies the fraction of emission into a waveguide mode propagating in a single direction as opposed to all other optical modes. This can also be written $\beta_{\text{dir}} = \beta F_{\text{dir}}$, where $\beta = \Gamma_{\text{wg}}/(\Gamma_{\text{wg}} + \gamma_{\text{rad}})$, and $F_{\text{dir}} = \max[\Gamma_R, \Gamma_L]/\Gamma_{\text{wg}}$.

We investigate a photonic-crystal waveguide with a glide-plane symmetry [11, 12], and show that the modes of such a glide-plane waveguide (GPW) have electric fields that are circularly polarized (for details of the waveguide design see the Supplementary Material). The band structure is shown in Fig. 1(a) with the band of interest highlighted in red. Using a finite element frequency domain method we calculate F_{dir} as a function of position as shown in Fig. 1(b) and the spatial map of β_{dir} , cf. Fig.1(c). We emphasize that positions with highly chiral spin-photon interaction are very abundant in the GPW as opposed to the case of regular PCWs where it is found in polarization singularity points [13]. The frequency dependence of β_{dir} is shown in Fig. 1(d). The oscillations in the directionality are due to small reflections at the out-coupling waveguides at the edge of the computation domain. $\beta_{\text{dir}} > 0.9$ is found for the entire frequency range corresponding to a bandwidth of ~ 70 nm at 920 nm. Modes with circular polarization have recently been observed in bottle resonators inter-

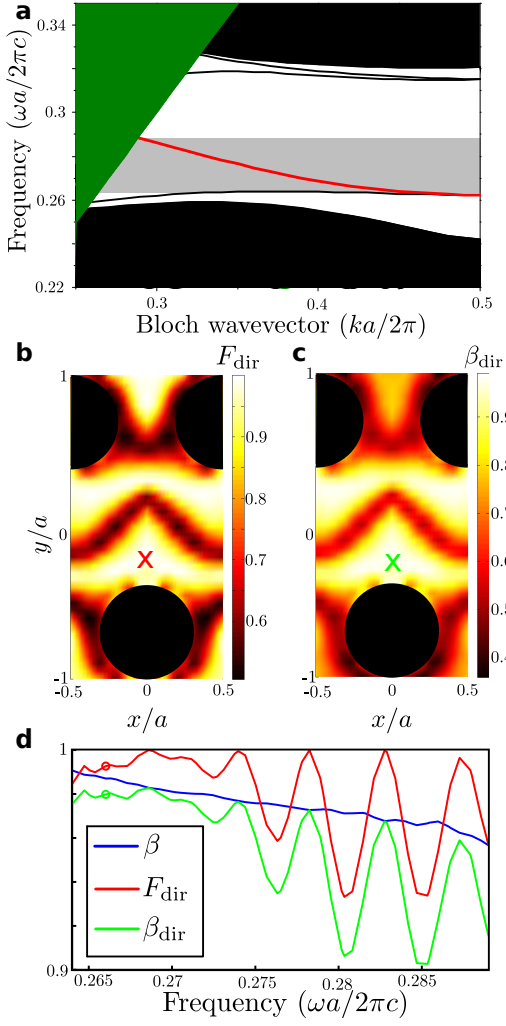


FIG. 1. (a) Band diagram of the GPW (see supplementary material for the detailed parameters of GPW) with the mode of interest in red and bandwidth in grey shading. Black lines and shading indicate other modes, while the green shading is the continuum of radiation modes. (b) Directionality factor F_{dir} , and (c) directional β -factor β_{dir} of the GPW at frequency $\omega a/2\pi c = 0.266$ (circles in (d)). A value of $F_{\text{dir}} = 0.5$ corresponds to positions where a circularly polarized dipole couples equally to both propagation directions, while $F_{\text{dir}} = 1$ corresponds to perfect unidirectional radiation. The blacked out circles indicate the position of the air holes. (d) Frequency sweep of β , F_{dir} , and β_{dir} , at the position denoted by the cross in (b) and (c). Note that all three values fall within the range 0.9-1 for the entire frequency range investigated.

faced with atoms [14]. In these systems, the maximum value of F_{dir} is bounded by the refractive index of the resonator material, while here it approaches unity and is very broadband. Finally, we note that a mode with circular polarization cannot exist in a standing wave cavity and that such a polarization scheme is unique to propagating modes.

A linearly polarized π -pulse on resonance with the de-

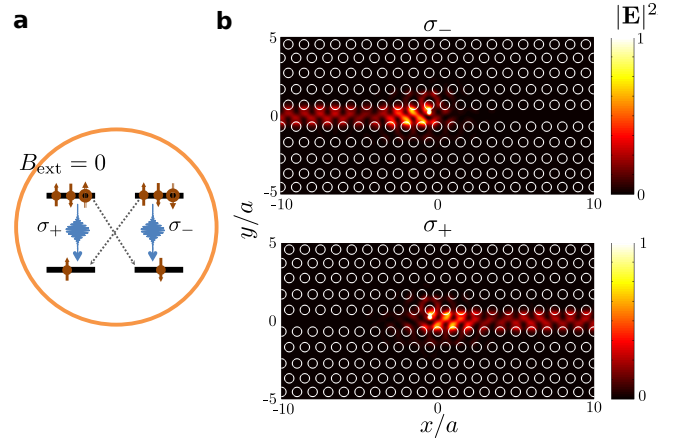


FIG. 2. (a) Two degenerate circularly polarized transitions of a trion in the absence of any magnetic field. The dashed diagonal lines indicate the dipole-“forbidden” transitions. (b) Directional emission of a QD placed in a GPW depending on the polarization.

generate trion transitions transfers the QD population into one of the two excited states depending on the initial spin orientation of the ground state as shown in Fig. 2(a). The propagation direction of the ensuing emission is strongly correlated with the polarization of the transition dipole of the decay channel as in Fig. 2(b). The probability that a photon emitted from the σ_- -transition propagates towards the left (top panel of Fig. 2(b)) is $P_L = \beta_{\text{dir}}$ while the probability of the photon emitted from the same transition propagating towards the right is $P_R = \beta - \beta_{\text{dir}}$. Preparing the ground state in a superposition of spin states can produce a spin-path entangled state. This can be extended to produce a one-dimensional photonic cluster state [15] (see Supplementary Material).

An alternative to operating in the regime of spontaneous emission is the coherent-scattering regime, which dominates the scattering processes for narrow-band single photons that has been shown to be robust against decoherence mechanisms [16]. This scattering process has been thoroughly studied theoretically in conventional waveguides coupled to two-level emitters [17, 18]. The transmission coefficient for a monochromatic single photon with energy $\hbar\omega_k$ through the chiral QD-waveguide system is

$$\bar{t}_k = \frac{\omega_k - \omega_{ge} - i(\Gamma_{\text{dir}} - \gamma)/2}{\omega_k - \omega_{ge} + i(\Gamma_{\text{dir}} + \gamma)/2}, \quad (2)$$

where Γ_{dir} is the decay rate into the preferred direction of the waveguide mode, $\hbar\omega_{ge}$ is the energy difference between ground and first excited state, and $\gamma = (1 - F_{\text{dir}})\Gamma_{\text{wg}} + \gamma_{\text{rad}}$ is the decay rate into loss modes. The first term in γ corresponds to coupling to the counter-propagating mode due to the polarization not being

purely circular, while γ_{rad} is the rate of coupling to non-guided radiation modes. We note that the above transmission coefficient for the chiral QD-waveguide system is equivalent to that of a QD in a conventional waveguide in the even-mode picture, i.e. when the photon is in an even superposition of counter-propagating modes [18]. Interacting with a quantum emitter in the even mode is the basis for the operation of many proposed devices [19–21]. The transmission amplitude for narrow-band resonant photons scales as $|1 - 2\beta_{\text{dir}}|$ and a π -phase shift is imparted on the transmitted photon for all $\Gamma_{\text{dir}} > \gamma$ (i.e. $\beta_{\text{dir}} > 0.5$). This phase shift combined with the near-perfect transmission found for high β_{dir} form the basis of the applications introduced here.

The applications we outline below all exploit the level structure of a singly-charged exciton (trion) placed in an external magnetic field pointing along the growth direction of the sample. The energy levels of the charged QD in such a magnetic field are shown in Fig. 3(c). The non-zero branching ratio, indicated by the two dashed diagonal lines in Fig. 3(c), limits the theoretically achievable β -factor setting an upper-bound on the success probability of the applications discussed below. Importantly, the decay rate of the diagonal transition Γ_{diag} can be suppressed by a magnetic field in the growth direction B_{ext} [22]. A branching ratio of approximately 1:1000 was extracted for $B_{\text{ext}} = 300$ mT [5, 22]. For magnetic fields above 2 T, the spin relaxation time has been experimentally shown to decrease as B_{ext}^{-5} [23], as predicted for single-phonon assisted spin-orbit coupling [24, 25]. These two effects set the boundaries for the range of external magnetic fields used for the suggested application. A detailed characterization of an individual QD is necessary to find the ideal value for a given application.

By integrating the GPW into an on-chip Mach-Zehnder Interferometer (MZI) the spin ground state of a charged QD can be read out by a single photon. This enables efficient spin read-out without optically pumping the spin to another state. The MZI is illustrated by the blue circuit in Fig. 3(d). The arms are balanced so that a single photon incident in arm **1** exits through arm **4**. A single photon propagating along path **A** and on resonance with the blue transition acquires an additional π -phase shift relative to a photon propagating along path **B**, if the QD is in the spin-up ($|\uparrow\rangle$) ground-state. This results in the single photon incident in arm **1** exiting through arm **3**, while a single photon incident when the QD is in the state $|\downarrow\rangle$ exits in arm **4**. This constitutes an on-chip readout of the QD-spin state with a single photon. Any reduction of the directional β -factor, β_{dir} , leads to a lower total transmission (photon loss) and to a reduced MZI-visibility. A non-unity visibility causes errors in the spin readout, by incorrectly channelling a fraction of photons into arm **4** even though the QD is in the state $|\uparrow\rangle$. The spin qubit in the state $|\downarrow\rangle$ is always detected perfectly for a large splitting between the two

transition energies by the external magnetic field B_{ext} . In the limit of spectrally narrow single photons, the probabilities of a successful spin readout, a false spin readout, and of photon loss are given by $P_s \sim (\beta_{\text{dir}}^2 + 1)/2$, $P_{\text{err}} \sim (1 - \beta_{\text{dir}})^2/2$, and $P_{\text{loss}} \sim \beta_{\text{dir}} - \beta_{\text{dir}}^2$ respectively. The exact solutions to these probabilities for a single-photon pulse of a finite spectral width are detailed in the Supplementary Material. Finally, we note that spin readout interaction can be viewed as a cNOT gate between the spin state and the photon.

Adding coherent control of the single electron spin qubit, allows creating arbitrary superpositions of the two single electron ground-states. Such control can be achieved both by optical methods [2, 3] and through in-plane oscillating magnetic fields $B_{\mu\text{w}}$ created by a microwave source [26], as shown schematically in Fig. 3(c). Using this control, a single-photon quantum non-demolition (QND) detector can be built by following the method proposed in Ref. [20]. The spin qubit is initialized in the state $|\uparrow\rangle$ through optical spin pumping [5] by driving the red transition. Using the field $B_{\mu\text{w}}$, a $\pi/2$ -rotation of the spin qubit puts it in a superposition state. A single photon on resonance with the blue transition, $|k_b\rangle$, only obtains a phase shift when the QD is in the state $|\uparrow\rangle$. After the single photon has past the interaction region a $-\pi/2$ rotation of the spin qubit is made. When a single photon passes the interaction region, the total sequence is as follows

$$\begin{aligned}
 |\uparrow\rangle &\xrightarrow{\pi/2} \frac{1}{\sqrt{2}} (|\uparrow\rangle + |\downarrow\rangle) \xrightarrow{k_b} \frac{1}{\sqrt{2}} (\bar{t}_k |\uparrow, k_b\rangle + |\downarrow, k_b\rangle) \\
 &\xrightarrow{-\pi/2} \frac{1}{2} [(\bar{t}_k + 1)|\uparrow\rangle + (1 - \bar{t}_k)|\downarrow\rangle] |k_b\rangle. \quad (3)
 \end{aligned}$$

In the second step of this sequence it is essential that the photon-matter state is separable after the interaction. In the ideal case $\bar{t}_k \rightarrow -1$, and one of the spin-states acquires a π -phase shift due to the interaction with the emitter and thus the original spin state is recovered when a photon passes the interaction region while the spin state is flipped when no photon passes. Assuming perfect initialization, control, and readout of the spin state, the success probability of the QND measurement scales as β_{dir}^2 . The final spin-state can be read out by either exciting the QD with π -pulses or using a stream of single photons or a weak coherent state.

We now combine the single photon spin read-out with the QND detector to form a deterministic controlled NOT (cNOT) gate, where a single control photon controls the state of a target photon. We note that a similar scheme can also be used to create a single-photon transistor/switch. The circuit for the cNOT gate is shown in Fig. 3(a). The QD is embedded in the GPW, which is adiabatically tapered to efficiently couple to a ridge waveguide as shown in Fig. 3(b)-(d). The external magnetic field B_{ext} splits the transitions and decreases the rate of diagonal transitions. The cNOT gate requires control

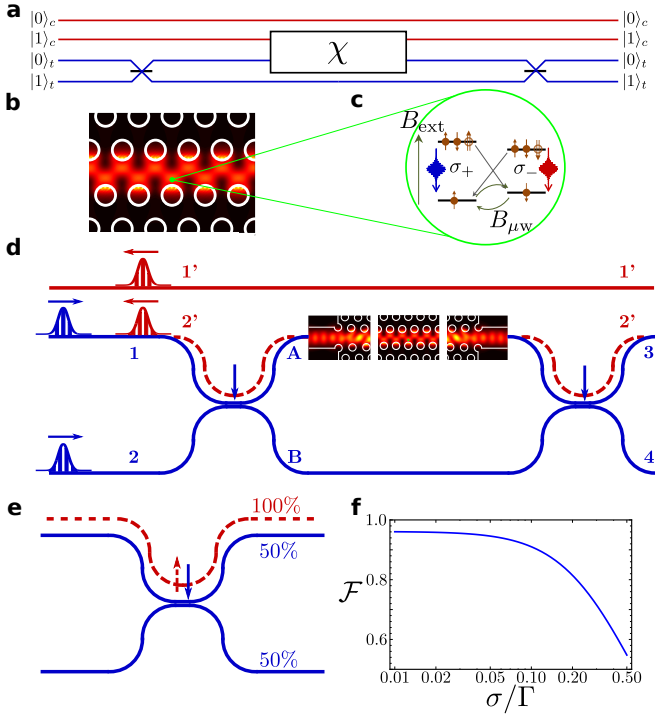


FIG. 3. (a) Schematic of a cNOT gate with a chiral element χ used to impart a conditional π -phase shift. (b) Electric field intensity of a mode propagating through a GPW. A QD is positioned at a point of high β_{dir} within the waveguide mode forming a chiral spin-photon interface. (c) Level scheme of the charged QD coupled to the GPW. A magnetic field along the growth direction B_{ext} splits the two circularly polarized transitions, denoted in blue and red. Coherent control of the spin qubit is obtained through an oscillating in-plane magnetic fields, generated by a microwave source on resonance with the electron spin transition, $B_{\mu\omega}$. (d) Schematic of the actual implementation of cNOT gate with reconfigurable beam splitter and chiral spin-photon interface. A control photon in an arbitrary superposition state (red wavepacket) passes the QD, and the beam splitters are subsequently configured to be 50:50 couplers. A photon in a superposition state of the two blue arms is then entering the circuit, where a transition PCW region is implemented in order to couple from the ridge waveguide to the GPW. (e) Schematic of a reconfigurable beam splitter. An actuator pulls apart the arms of the beam splitter to suppress coupling (dashed red), or brings arms together to form a 50:50 beam splitter (blue). (f) Entangling fidelity \mathcal{F} of the proposed cNOT gate as a function of normalized photon pulse width $\sigma_{\text{lor}}/\Gamma$ for $\beta_{\text{dir}} = 0.98$.

and target photons to interact sequentially with the QD. This can be achieved using a reconfigurable beam splitter [27] as shown in Fig. 3(e). The distance between the two arms of the beam splitter is reconfigured to alternate between 100:0 and 50:50 coupling. The reconfigurable beam splitter allows us to map the spatial modes $|1\rangle_c$ and $|0\rangle_t$ to distinct temporal modes as shown in Fig. 3(d). The red photons pass through the circuit first, the beam splitters are then reconfigured to 50:50 coupling, and then

the blue photons enter the circuit. We note that because the QDs optical transitions have orthogonal circular polarization, the control and target photons propagate in opposite directions.

The following sequence is used to implement the cNOT gate:

1. The process for the QND detection is followed for the control qubit, but the photon is now resonant with the red transition. If the control photon is in arm **2'** the spin is mapped to $|\downarrow\rangle$, while if the photon is in arm **1'** the spin remains in $|\uparrow\rangle$.
2. A single photon incident in arm **1** now exits in arm **4** if the control photon was in arm **2'**, while it exits in arm **3** for the control photon in arm **1'**.
3. A quantum eraser protocol is employed: a $\frac{\pi}{2}$ rotation on the QD spin is followed by a measurement of the spin state. A π -phase is imparted on arm **2'** on the condition of measuring $|\uparrow\rangle$.

The computational basis of this cNOT-gate is given by the control qubit, $|0_c\rangle = \mathbf{1}'$ and $|1_c\rangle = \mathbf{2}'$, and the target qubit, $|0_t\rangle = (\mathbf{1}, \mathbf{3})$ and $|1_t\rangle = (\mathbf{2}, \mathbf{4})$. We note that the final step is required to disentangle the spin state from the optical state [28]. The measurement can be done by reading out the spin state using a weak coherent state, which introduces no additional errors. Detailed calculations for the performance of the cNOT gate are presented in the Supplementary Material. Here we present the fidelity \mathcal{F} of an entanglement process and the minimum fidelity \mathcal{F}_{min} for the gate. For an ideal cNOT gate the input state $(|0_c\rangle + |1_c\rangle)|0_t\rangle/\sqrt{2}$ produces the maximally entangled Bell state $|\Phi^-\rangle$ as an output. The modulus square of the overlap of the output state $|\text{out}\rangle$ with the output of the ideal gate gives the fidelity $\mathcal{F} = |\langle\Phi^-|\text{out}\rangle|^2 = \beta_{\text{dir}}^2$. We have shown that values of $\beta_{\text{dir}} \sim 0.98$ can be achieved simultaneously for both transitions in our PCW corresponding to $\mathcal{F} = 0.96$ for an entanglement process. The fidelity with $\beta_{\text{dir}} = 0.98$ is shown for single photons with different Lorentzian pulse widths σ_{lor} in Fig. 3(f). For $\sigma_{\text{lor}} < 0.1\Gamma$, $\mathcal{F} > 0.91$. The gate operates at its lowest fidelity for the input state $|0_c\rangle(i|0_t\rangle + |1_t\rangle)/\sqrt{2}$, giving $\mathcal{F}_{\text{min}} = (1 - 2\beta_{\text{dir}})^2$. For narrow-band pulses with $\beta_{\text{dir}} = 0.98$ this gives a minimum fidelity $\mathcal{F}_{\text{min}} = 0.92$.

We have introduced a PCW whose modes have a strong in-plane circular polarization and have shown that a coupled QD forms a chiral spin-photon interface. This can be used for single-photon spin readout, to construct a QND photon detector, and for a cNOT gate. This may form the basis for a fully scalable solid-state quantum-photonics architecture. While we here focused on applications with QDs, the proposed waveguide would readily be applicable to colour centres in diamond photonics and the underlying design principles can likely be extended to nanophotonic waveguides interfaced with single atoms.

One of the technical challenges particular to realizing this cNOT gate is to implement reconfigurable beam splitters. Using emitters where the two transitions have a larger detuning, such as those present in QD molecules [29], could allow for the two transitions to be separated using passive frequency selective add-drop filters [30].

The authors would like to thank Anders Sørensen, Leonardo Midolo and Dirk Witthaut for useful discussions.

During the final stage of preparing the manuscript, two related works have appeared. Ref. [31] considers directional coupling in a reflection-symmetric photonic-crystal waveguide and no quantum gates are proposed. Ref. [32] considers the case of single atoms coupled to the evanescent field of a tapered optical fiber, where pronounced directional photon emission is observed.

* These authors contributed equally

† lodahl@nbi.ku.dk; www.quantum-photonics.dk

- [1] M. Kroutvar, Y. Ducommun, D. Heiss, M. Bichler, D. Schuh, G. Abstreiter, and J. J. Finley, *Nature* **432**, 81 (2004).
- [2] D. Press, T. D. Ladd, B. Zhang, and Y. Yamamoto, *Nature* **456**, 218 (2008).
- [3] A. Greilich, S. E. Economou, S. Spatzek, D. R. Yakovlev, D. Reuter, A. D. Wieck, T. L. Reinecke, and M. Bayer, *Nat. Phys.* **262**, 262 (2009).
- [4] A. N. Vamivakas, Y. Zhao, C.-Y. Lu, and M. Atatüre, *Nat. Phys.* **5**, 198 (2009).
- [5] S. T. Yilmaz, P. Fallahi, and A. Imamoglu, *Phys. Rev. Lett.* **105**, 033601 (2010).
- [6] T. Yoshie, A. Scherer, J. Hendrickson, G. Khitrova, H. M. Gibbs, G. Rupper, C. Ell, O. B. Shchekin, and D. G. Deppe, *Nature* **432**, 200 (2004).
- [7] M. Arcari, I. Söllner, A. Javadi, S. L. Hansen, J. Liu, H. T. Nielsen, E. H. Lee, J. D. Song, S. Stobbe, and P. Lodahl, *arXiv:1402.2081* (2014).
- [8] P. Lodahl, S. Mahmoodian, and S. Stobbe, *arXiv:1312.1079* (2013).
- [9] I. J. Luxmoore, N. A. Wasley, A. J. Ramsay, A. C. T. Thijssen, R. Oulton, M. Hugues, S. Kasture, V. G. Achanta, A. M. Fox, and M. S. Skolnick, *Phys. Rev. Lett.* **110**, 037402 (2013).
- [10] A. Majumdar, P. Kaer, M. Bajcsy, E. D. Kim, K. G. Lagoudakis, A. Rundquist, and J. Vučković, *Phys. Rev. Lett.* **111**, 027402 (2013).
- [11] J. S. Brownless, S. Mahmoodian, K. B. Dossou, F. J. Lawrence, L. C. Botten, and C. M. de Sterke, *Opt. Express* **18**, 25346 (2010).
- [12] A. Mock, L. Lu, and J. O'Brien, *Phys. Rev. B* **81**, 155115 (2010).
- [13] M. Burrelli, R. J. P. Engelen, A. Opheij, F. van Oosten, D. Mori, T. Baba, and L. Kuipers, *Phys. Rev. Lett.* **102**, 033902 (2009).
- [14] C. Junge, D. O'Shea, J. Volz, and A. Rauschenbeutel, *Phys. Rev. Lett.* **110**, 213604 (2013).
- [15] N. H. Lindner and T. Rudolph, *Phys. Rev. Lett.* **103**, 113602 (2009).
- [16] C. Matthiesen, M. Geller, C. H. H. Schulte, C. L. Gall, J. Hansom, Z. Li, M. Hugues, E. Clarke, and M. Atatüre, *Nat. Commun.* **4** (2013).
- [17] J. T. Shen and S. Fan, *Opt. Lett.* **30**, 2001 (2005).
- [18] S. Fan, Şükruü Ekin Kocabaş, and J.-T. Shen, *Phys. Rev. A* **82**, 063821 (2010).
- [19] D. E. Chang, A. S. Sørensen, E. A. Demler, and M. D. Lukin, *Nat. Phys.* **3**, 807 (2007).
- [20] D. Witthaut, M. D. Lukin, and A. S. Sørensen, *Europhys. Lett.* **97**, 50007 (2012).
- [21] M. Bradford, K. C. Obi, and J.-T. Shen, *Phys. Rev. Lett.* **108**, 103902 (2012).
- [22] J. Dreiser, M. Atatüre, C. Galland, T. Müller, A. Badolato, and A. Imamoglu, *Phys. Rev. B* **77**, 075317 (2008).
- [23] C.-Y. Lu, Y. Zhao, A. N. Vamivakas, C. Matthiesen, S. Fält, A. Badolato, and M. Atatüre, *Phys. Rev. B* **81**, 035332 (2010).
- [24] A. V. Khaetskii and Y. V. Nazarov, *Phys. Rev. B* **64**, 125316 (2001).
- [25] L. M. Woods, T. L. Reinecke, and Y. Lyanda-Geller, *Phys. Rev. B* **66**, 161318 (2002).
- [26] M. Kroner, K. M. Weiss, B. Biedermann, S. Seidl, S. Manus, A. W. Holleitner, A. Badolato, P. M. Petroff, B. D. Gerardot, R. J. Warburton, and K. Karrai, *Phys. Rev. Lett.* **100**, 156803 (2008).
- [27] Y. Akihama, Y. Kanamori, and K. Hane, *Opt. Express* **19**, 23658 (2011).
- [28] A. Reiserer, N. Kalb, G. Rempe, and S. Ritter, *Nature* **508**, 237 (2014).
- [29] A. N. Vamivakas, C.-Y. Lu, C. Matthiesen, Y. Zhao, S. Fält, A. Badolato, and M. Atatüre, *Nature* **467**, 297 (2010).
- [30] V. Veerasubramanian, G. Beaudin, A. Gigure, B. L. Drogoff, V. Aimez, and A. G. Kirk, *Opt. Express* **20**, 15983 (2012).
- [31] A. B. Young, A. Thijssen, D. M. Beggs, L. Kuipers, J. G. Rarity, and R. Oulton, *arXiv:1406.0714* (2014).
- [32] R. Mitsch, C. Sayrin, B. Albrecht, P. Schneeweiss, and A. Rauschenbeutel, *arXiv:1406.0896* (2014).

SUPPLEMENTARY MATERIAL

Glide-plane waveguides

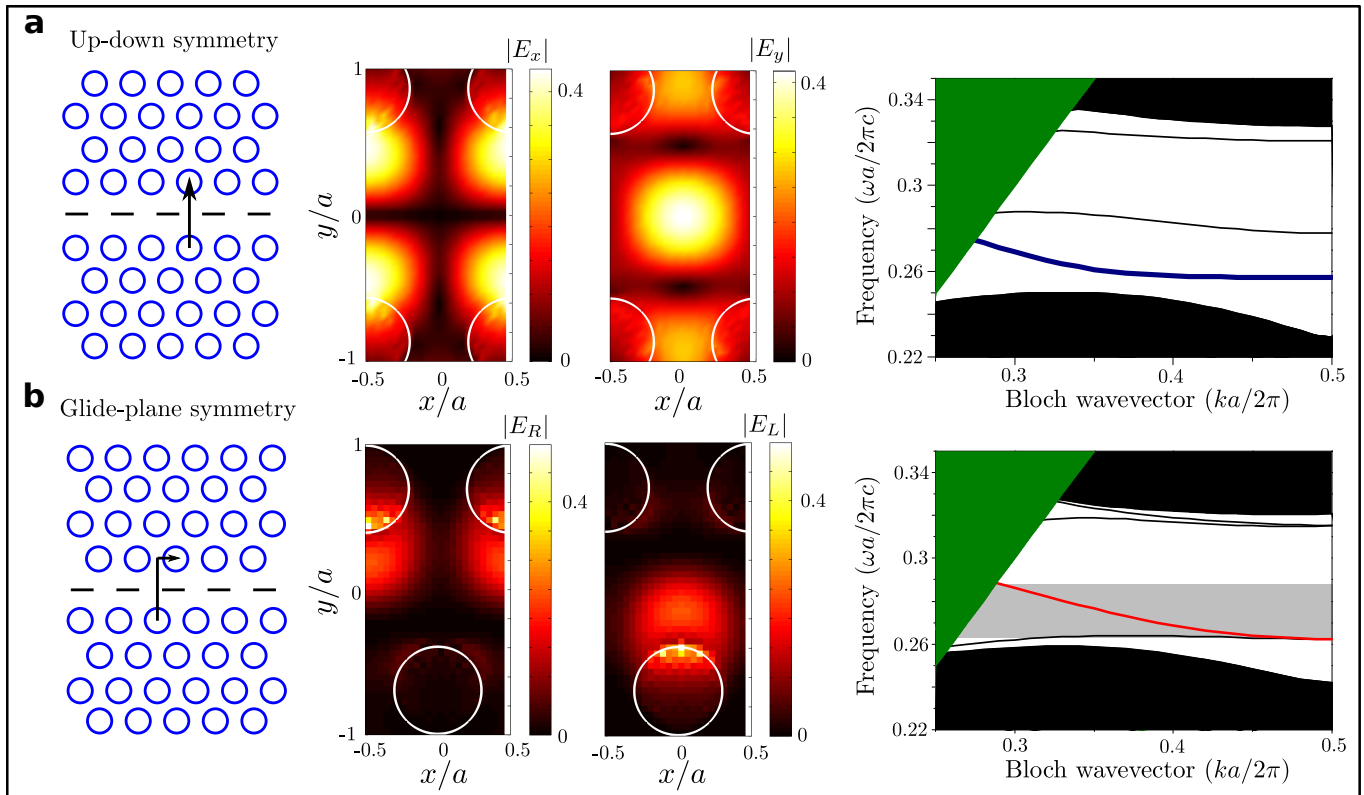


FIG. 4. (a) Schematic of a standard W1 PCW (top-left) with reflection symmetry about $y = 0$. The magnitude of the electric field components E_x and E_y (top-centre) are shown for a W1 waveguide with refractive index $n = 3.46$, hole radius $r = 0.3a$, membrane thickness $t = 0.6a$ where a is the lattice period. The band diagram of this waveguide is also shown (top-right). Here the blue line shows what is usually the band of interest, the black lines and shading show other bands and continuum, while the green shading shows the radiation modes. (b) Schematic of a glide-plane symmetry waveguide (bottom-left) with the magnitude of the right and left hand circularly polarized electric field components E_R and E_L respectively (bottom-centre). The band diagram (parameters in text) of this waveguide is shown (bottom-right) with the band of interest highlighted in red. The grey region shows the frequency range for which β_{dir} is computed in Fig. 1(d) in the main text.

In this section we present the design of the glide plane waveguides used in the main text. To fully appreciate the performance of our proposed waveguide we briefly outline the QD-waveguide coupling process. The decay rate Γ of a QD coupled to a photonic mode depends on the projection of the transition dipole moment \mathbf{d} on the electric field at the position of the dipole $\mathbf{E}(\mathbf{r}_d)$ [1]

$$\Gamma \propto |\mathbf{E}(\mathbf{r}_d) \cdot \mathbf{d}|^2. \quad (4)$$

For on-chip spin readout we are interested in the coupling properties of the circular dipole transitions, i.e., $\hat{\mathbf{x}} \pm i\hat{\mathbf{y}}$, where x and y are the two symmetry directions of the QD and the photonic-crystal membrane. We are thus interested in structures whose modes have field maxima with a large degree of circular polarization. In a standard W1 PCW the mirror symmetry along the center of the waveguide ($y = 0$ plane) sets strict restrictions on the electric field of the propagating mode. Figure 4(a) shows a schematic of a conventional PCW that is up-down symmetric, i.e. invariant under reflection about the $y = 0$ plane. The eigenmodes of this waveguide have electric field distributions that are either odd or even about $y = 0$ (computed using plane-wave expansion software [2]). The magnitude of the electric field components are shown in Fig. 4(a). The y -component of the field E_y is an even function in y , while the x -component E_x is an odd function in y . The fields in such a waveguide are dominantly linearly polarized. Such a mode cannot have circularly polarized fields near its field maxima due to symmetry restrictions.

The waveguide proposed in this work is based on a glide plane symmetry and is shown schematically in Fig. 4(b). The geometry is invariant under a reflection about $y = 0$ followed by a half-period translation in the x -direction. Breaking the up-down symmetry leads to the waveguide modes having different polarization properties. Our design is based on a photonic crystal membrane with holes etched in a triangular lattice. The membrane has refractive index $n = 3.46$, hole radius $r = 0.3a$, and thickness $t = 0.6a$, where a is the lattice constant. The hole-to-hole center width of the waveguide is $0.8a\sqrt{3}$, and the second, third and fourth rows of holes have been shifted out by the respective distances $\Delta y_2 = 0.15a\sqrt{3}/2$, $\Delta y_3 = 0.2a\sqrt{3}/2$, and $\Delta y_4 = 0.1a\sqrt{3}/2$ with respect to the triangular lattice. Using a perturbative model, it has previously been shown [3] in coupled waveguides that, near the edge of the Brillouin zone, the eigenmodes of a glide-plane geometry can be expressed as a superposition of the symmetric eigenmodes with coefficients that are out of phase by $\pi/2$. The transition from a symmetric waveguide to a glide-plane waveguide cannot be treated perturbatively here, however the eigenstates of the glide-plane waveguide still have an electric field with an in-plane circular polarization that becomes more prevalent close to the Brillouin zone edge.

Spin-path entanglement and cluster state generation

A charged QD coupled to a glide-plane waveguide can be exploited to create spin-path entanglement between the QD electron spin and an emitted photon. The QD electron can be initialized in the spin-up $|\uparrow\rangle$ or spin-down $|\downarrow\rangle$ state by optical spin pumping [4] with an appropriate circularly polarized laser. This is followed by a $\pi/2$ -rotation of the spin to put it in a coherent superposition of the two ground-states. A π -pulse excitation leads to the emission of a single photon, the propagation direction of which is entangled with the spin

$$|\uparrow\rangle \xrightarrow{B_{xy,\pi/2}} \frac{1}{\sqrt{2}} (|\uparrow\rangle + |\downarrow\rangle) \xrightarrow{\pi} \frac{1}{\sqrt{2}} (|\uparrow, R\rangle + |\downarrow, L\rangle), \quad (5)$$

where $|L\rangle$ and $|R\rangle$ denote a left and a right propagating photon.

Following the proposal of Ref. [5], we envision using the Larmor precession of the spin ground state around a weak in-plane magnetic field B_{xy} to obtain the $\pi/2$ -rotation of the spin. This is done by precisely synchronising the pulsed resonant (π -pulse) excitation with the spin rotation in order to create a stroboscopic effect, which leads to the following pulse sequence, $B_{xy,\pi/2} \rightarrow \pi \rightarrow B_{xy,\pi/2} \rightarrow \pi \rightarrow \dots$. This sequence can be extended to efficiently produce a 1D cluster state as proposed in [5],

$$\begin{aligned} \frac{1}{\sqrt{2}} (|\uparrow, R_1\rangle + |\downarrow, L_1\rangle) &\xrightarrow{B_{xy,\pi/2}} \frac{1}{2} ((|\uparrow\rangle + |\downarrow\rangle) |R_1\rangle + (-|\uparrow\rangle + |\downarrow\rangle) |L_1\rangle) \\ &\xrightarrow{\pi_2} \frac{1}{2} ((|\uparrow\rangle |R_2\rangle + |\downarrow\rangle |L_2\rangle) |R_1\rangle + (-|\uparrow\rangle |R_2\rangle + |\downarrow\rangle |L_2\rangle) |L_1\rangle) \xrightarrow{B_{xy,\pi/2}} \dots \end{aligned} \quad (6)$$

The error on a detected photon is given by $P_{\text{det-err}} = \frac{P_{\text{err}}}{P_{\text{s}} + P_{\text{err}}} = 1 - F_{\text{dir}}$, while the photon loss is given by $P_{\text{loss}} = 1 - (P_{\text{s}} + P_{\text{err}}) = 1 - \beta$. Here we have only included the errors caused by the polarization-to-path transformation in the waveguide. A detailed discussion of other error sources is given in [5]. Due to the broadband nature of β_{dir} (see Fig. 1(d) in main text) this protocol can likely be extended to generate 2D photonic cluster states as proposed in [6].

Scattering photon wave-packets

In the main text we mainly considered photon wavepackets whose spectral width are very narrow in comparison to the QD natural linewidth. Here we relax this assumption and consider scattering of photons with a finite spectral width. We discuss this in the context of spin readout, but the theory is very similar for the QND photon detection and can also be extended to the cNOT gate. Here, we use the photon scattering theory presented in [7]. As shown in Fig. 5(a), the QD has a blue and red transition for each of the spin states. Here we consider the case where the input photon is targeting the blue transition. We use $|0_t\rangle$ and $|0_b\rangle$ for vacuum states of the top and bottom arms of the Mach-Zehnder interferometer (MZI) shown in Fig. 5(c) respectively. We consider a photon incident on the top arm of the MZI with a spectral profile $f(k)$ as the input state

$$|\Psi_{\text{in}}\rangle = \int dk f(k) \hat{a}_k^\dagger |0_t\rangle, \quad (7)$$

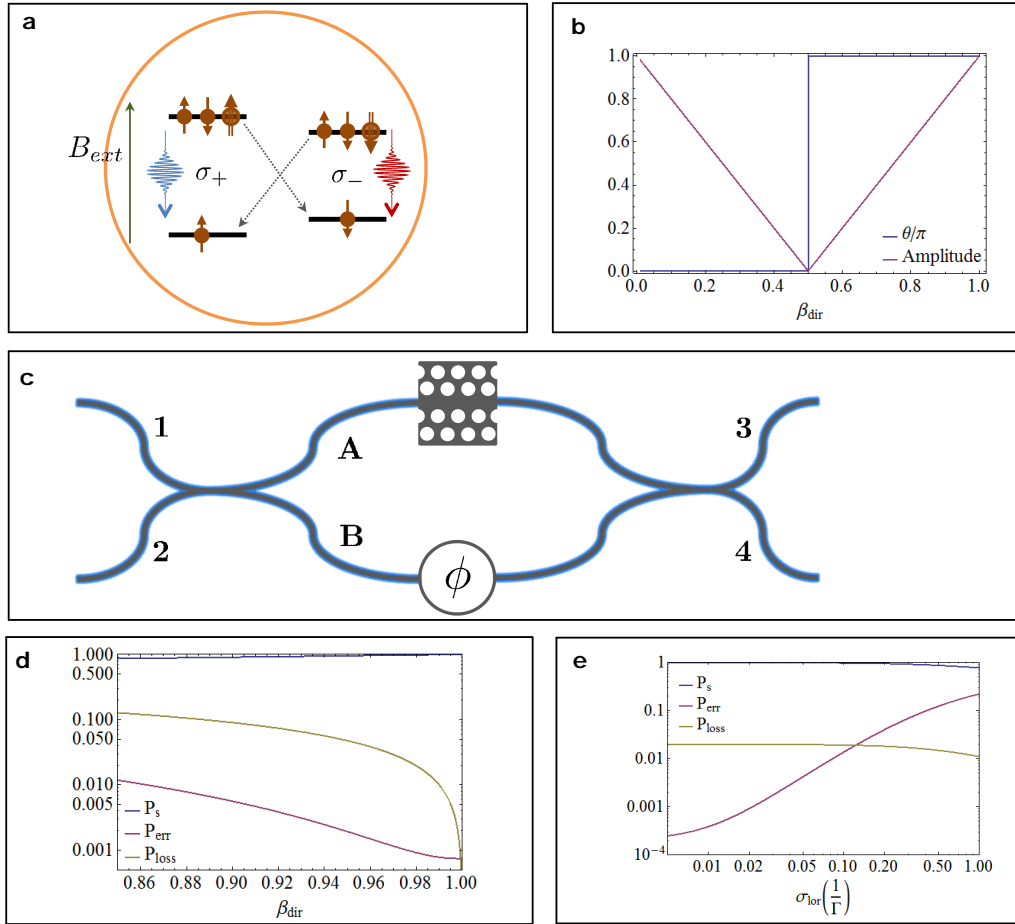


FIG. 5. (a) An external magnetic field, B_{ext} , along the growth direction splits the two circularly polarized transitions, denoted in blue and red. In addition to energetically splitting the two circular transitions the external magnetic field suppresses the diagonal transitions denoted by the gray dashed arrows. (b) The phase and probability amplitude for a single photon forward-scattered in a GPW as a function of the directional β -factor. (c) Schematic of the Mach-Zehnder interferometer suggested for on-chip spin readout. The interaction with the QD takes place in a section of the GPW placed in path **A**. Path **B** includes a phase control to ensure that the interferometer is correctly balanced. (d), The probabilities of a successful and of a false spin readout plotted along side the photon loss probability as a function of the directional β -factor. Here we assumed the incident single photon to have a Lorentzian spectral amplitude of width $\sigma_{\text{lor}} = 0.02\Gamma$. (e), The same three probabilities plotted as a function of the single-photon spectral width for $\beta_{\text{dir}} = 0.98$.

where \hat{a}_k^\dagger is the creation operator of a photon with energy k . Here we consider appropriately normalized Lorentzian spectral profiles of the form

$$f(k) = \frac{\sqrt{2\sigma_{\text{lor}}^3/\pi}}{\sigma_{\text{lor}}^2 + (k - k_0)^2}, \quad (8)$$

where σ is the pulse width and k_0 is the central energy of the pulse. The interaction with the beam splitter is expressed as a transformation by the unitary matrix

$$U = \frac{1}{\sqrt{2}} \begin{pmatrix} 1 & i \\ i & 1 \end{pmatrix}, \quad (9)$$

where the basis vectors $\hat{\mathbf{e}}_1$ and $\hat{\mathbf{e}}_2$ represent the states of the top and bottom arms respectively. Photons in the top arm scatter off the transition and obtain an energy dependent multiplicative factor t_k , while there is no interaction in the bottom arm. This is followed by another unitary transformation by the beam splitter. If the spin is in the state $|\downarrow\rangle$, for a perfect MZI, the photon always exits in the lower arm, and thus the spin is always measured correctly.

However, if the spin is in the state $|\uparrow\rangle$, a successful measurement occurs when the photon exits in the top arm, while an error occurs when the photon exits in the bottom arm. We define the total success probability of the spin readout as the average of the probabilities of measuring $|\uparrow\rangle$ and $|\downarrow\rangle$ correctly, with a corresponding definition for the error probability. The success, error and loss probabilities are shown for resonant photons ($k_0 = 0$) as a function of β_{dir} , and the pulse width σ_{lor} in Figs. 5(d)-(e). Here the loss probability is defined as the measurement being inconclusive as a results of the photon being scattered into a different mode. The procedure for computing the success probability for the quantum non-demolition detection of a photon is similar to the process outlined here. The success, error and loss probabilities are also similar to those shown here for the spin readout.

Performance of the cNOT gate

In this section we detail the success probability of the cNOT gate. We start by computing the fidelity of the cNOT gate as a function of β_{dir} for the input states $|0_c\rangle|0_t\rangle$, $|0_c\rangle|1_t\rangle$, $|1_c\rangle|0_t\rangle$, and $|1_c\rangle|1_t\rangle$. For each input state, the probability of the output state being $|0_c\rangle|0_t\rangle$, $|0_c\rangle|1_t\rangle$, $|1_c\rangle|0_t\rangle$, or $|1_c\rangle|1_t\rangle$ is shown in Tables I and II. Table I shows the probabilities for when the QD spin ends in the spin-up state while Table II shows probabilities for spin down. In the top left quadrant of these tables, the off-diagonal terms give the probability that the photon state is successfully switched by the gate. In the bottom right quadrant the diagonal terms are non-unity because when the control photon is switched off, the interaction in the MZI is switched on, therefore these terms signify the transmission probability of the MZI due to the presence of the emitter. In this table, we do not explicitly show the scattering into the different loss modes leading to the total probability in each row not summing to one. It is also assumed that all detector clicks are caused by photons in our circuit and additional errors will be produced in experimental realizations due to non-zero background and dark counts.

$ \uparrow\rangle$	$ 1_c, 1_t\rangle_{\text{out}}$	$ 1_c, 0_t\rangle_{\text{out}}$	$ 0_c, 1_t\rangle_{\text{out}}$	$ 0_c, 0_t\rangle_{\text{out}}$
$ 1_c, 1_t\rangle_{\text{in}}$	$(1 - \beta_{\text{dir}})^2 \beta_{\text{dir}}^2$	$(1 - \beta_{\text{dir}} + \beta_{\text{dir}}^2)^2$	0	0
$ 1_c, 0_t\rangle_{\text{in}}$	$(1 - \beta_{\text{dir}} + \beta_{\text{dir}}^2)^2$	$(1 - \beta_{\text{dir}})^2 \beta_{\text{dir}}^2$	0	0
$ 0_c, 1_t\rangle_{\text{in}}$	0	0	β_{dir}^2	$(1 - \beta_{\text{dir}})^2$
$ 0_c, 0_t\rangle_{\text{in}}$	0	0	$(1 - \beta_{\text{dir}})^2$	β_{dir}^2

TABLE I. Truth table for cNOT gate when the QD spin is measured in the $|\uparrow\rangle$ state.

$ \downarrow\rangle$	$ 1_c, 1_t\rangle_{\text{out}}$	$ 1_c, 0_t\rangle_{\text{out}}$	$ 0_c, 1_t\rangle_{\text{out}}$	$ 0_c, 0_t\rangle_{\text{out}}$
$ 1_c, 1_t\rangle_{\text{in}}$	$(1 - \beta_{\text{dir}})^2 \beta_{\text{dir}}^2$	$(1 - 3\beta_{\text{dir}} + \beta_{\text{dir}}^2)^2$	0	0
$ 1_c, 0_t\rangle_{\text{in}}$	$(1 - 3\beta_{\text{dir}} + \beta_{\text{dir}}^2)^2$	$(1 - \beta_{\text{dir}})^2 \beta_{\text{dir}}^2$	0	0
$ 0_c, 1_t\rangle_{\text{in}}$	0	0	β_{dir}^2	$(1 - \beta_{\text{dir}})^2$
$ 0_c, 0_t\rangle_{\text{in}}$	0	0	$(1 - \beta_{\text{dir}})^2$	β_{dir}^2

TABLE II. Truth table for cNOT gate when the QD spin is measured in the $|\downarrow\rangle$ state.

Now we consider scattering of photons with a finite pulse length. Following the theory presented for the spin readout, we have computed the entanglement fidelity \mathcal{F} (see main text for definition) as a function of β_{dir} and pulse width σ_{lor} . This is shown in Fig. 6. The white region shows the parameters for which $\mathcal{F} > 0.9$. With our value of $\beta_{\text{dir}} = 0.98$ we are able to achieve this for spectral pulse widths $\sigma_{\text{lor}} < 0.1\Gamma$.

* These authors contributed equally

† lodahl@nbi.ku.dk; www.quantum-photonics.dk

[1] P. Lodahl, S. Mahmoodian, and S. Stobbe, arXiv:1312.1079 (2013).

[2] S. G. Johnson and J. D. Joannopoulos, Opt. Express **8**, 173 (2001).

[3] J. S. Brownless, S. Mahmoodian, K. B. Dossou, F. J. Lawrence, L. C. Botten, and C. M. de Sterke, Opt. Express **18**, 25346 (2010).

[4] S. T. Yilmaz, P. Fallahi, and A. Imamoglu, Phys. Rev. Lett. **105**, 033601 (2010).

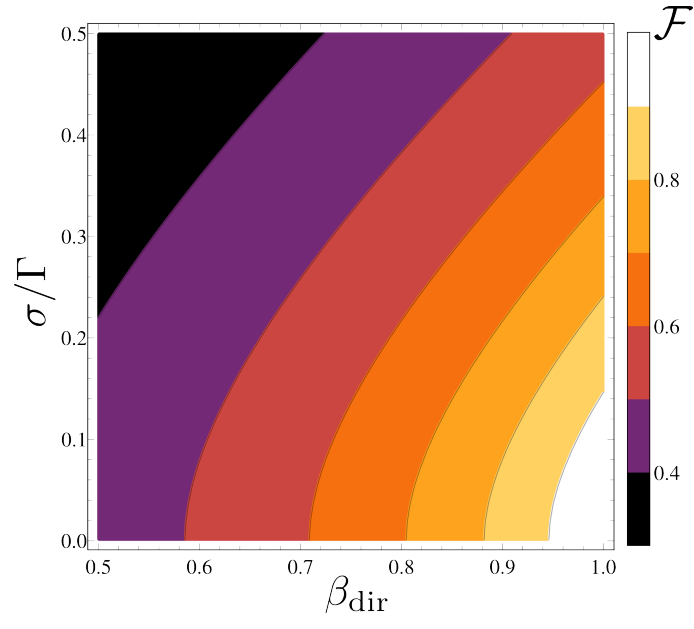


FIG. 6. Entanglement fidelity \mathcal{F} of the cNOT gate as a function of β_{dir} and pulse width $\sigma_{\text{lor}}/\Gamma$.

- [5] N. H. Lindner and T. Rudolph, Phys. Rev. Lett. **103**, 113602 (2009).
- [6] S. E. Economou, N. Lindner, and T. Rudolph, Phys. Rev. Lett. **105**, 093601 (2010).
- [7] S. Fan, S. E. Kocabaş, and J.-T. Shen, Phys. Rev. A **82**, 063821 (2010).